Shock Waves (2021) 31:379–398
https://doi.org/10.1007/s00193-021-01024-8

ORIGINAL ARTICLE

Propagation of spherical weak blast waves over rough periodic surfaces

T. Lechat[1] · A. Emmanuelli[1] · D. Dragna[1] · S. Ollivier[1]

Received: 17 November 2020 / Revised: 31 May 2021 / Accepted: 21 June 2021 / Published online: 12 July 2021

Abstract
Spherical weak blast propagation above a rough periodic surface is investigated by performing numerical simulations of the Euler equations. The study of the reflection pattern shows that waves diffracted by the surface asperities merge to form an effective reflected shock. It is initially detached from the incident shock but gradually catches up with it. If the source energy is sufficient, the reflected shock interacts with the incident one and Mach reflection occurs. Thus, the triple point has a similar trajectory to that over a smooth surface. In addition, the maximal overpressure is shown to be greater for small roughness scales in a layer near the surface. Far from the surface, it is close to that of a smooth surface for small roughness scales and to the free field for the highest ones. The increase in the maximal overpressure is related to oscillations on the waveforms that appear behind the shock. These properties are associated with the existence of a surface wave that propagates along the surface. Comparison of results in the linear regime with an analytic solution confirms this explanation.

Keywords Shock wave · Rough surface · Blast wave · Surface wave · Triple point

1 Introduction

When spherical blast waves propagate in outdoor environments, they interact with the inhomogeneities of the atmosphere as well as with the ground. The reflection of a spherical shock wave over a flat smooth impermeable and rigid ground surface is well documented in the literature (for instance, [1,2]). The reflection pattern is at first a regular reflection: The incident and reflected shocks intersect on the ground and the angle of reflection usually differs from the angle of incidence. At larger distances, the reflected shock catches up with the incident shock; the point of intersection is no longer on the surface but above and a third shock, named the Mach stem, is formed near the surface. The Mach stem then grows with the shock wave propagation. The slopes of the three shocks at the triple point are first different, and the reflection pattern is referred to as Mach reflection. The slopes of the Mach stem and the incident shock then become equal, corresponding to the von Neumann reflection.

However, actual outdoor surfaces are neither flat nor impermeable, nor rigid, nor smooth. Among the surface properties, roughness was shown to have a significant effect on the reflection of spherical blast waves. Dewey and colleagues [3,4] have investigated the characteristics of spherical blast wave reflection over an ideal surface and two real surfaces. For this, they use two identical explosive charges of approximately 500 kg of pentolite and consider the plane midway of the two charges as a plane of symmetry. The shock along this plane thus corresponds to a shock that would be reflected over an ideal surface. With the help of a painted backdrop or smoke puffs, a high-speed camera was used to determine the shock trajectories, and Rankine–Hugoniot relations were employed to deduce the pressure jump from the measurements of the shock speed. The shock characteristics for the ideal surface were compared to those measured for two ground surfaces: a smooth one and a rough one that was obtained by furrowing in a circular pattern the smooth surface. It was observed that the peak pressure along the ground and the length of the Mach stem were reduced for real surfaces compared to the ideal one, especially for the rough ground.

The characteristics of real ground in terms of roughness or absorption can hardly be measured with precision, in

Communicated by A. Hadjadj.

✉ D. Dragna
didier.dragna@ec-lyon.fr

[1] Laboratoire de Mécanique des Fluides et d'Acoustique, UMR5509, Univ Lyon, Ecole Centrale de Lyon, CNRS, Univ Claude Bernard Lyon 1, INSA Lyon, 69130 Ecully, France

particular over a large surface area. Consequently, outdoor experiments provide valuable information but it is mostly qualitative. An alternative to study the roughness effects of spherical blast wave reflection is to perform controlled experiments, in which the roughness can be known precisely. The first study at laboratory scale was carried out by Huber and McFarland [5]. Blast waves were generated by a small explosive charge, and measurements were taken along a propagation line using flush-mounted surface microphones and schlieren optical systems. Both a smooth surface and a rough surface made of pyramid-shaped elements of 3.2-mm height and 6.4-by-6.4-mm base were considered. It was found that with the rough surface, the peak overpressure at the surface was slightly reduced, the formation of the Mach stem was delayed, and the Mach stem height was reduced compared to the smooth surface case, in agreement with Dewey et al. [3]. These are the main conclusions reported in Needham [6] on the effects of roughness on blast wave propagation.

Experiments on the reflection of spherical shock waves on a flat plane at laboratory scale have been recently reported [7,8]. ln Karzova et al. [7], an electric spark source was used to generate weak shock waves, with characteristics typical of blast waves. The waveform duration was about 50 μs corresponding to a wavelength of 20 mm. A significant contribution of the study was the measurement of the pressure waveforms thanks to a Mach–Zehnder optical interferometry method. Three different surface conditions were considered: a smooth surface and two rough surfaces made of sandpaper with correlation lengths of 0.18 and 0.34 mm. In accordance with previous studies, it was noted that roughness induces a reduction in the Mach stem height. For the largest roughness scale, the Mach stem did not appear. In addition, close to the surface, the waveforms for a rough surface exhibit oscillations, whose pattern depends on the roughness scale. Interestingly, these oscillations lead to an increase in peak overpressure compared to a smooth surface, which seems to contradict the previously mentioned experiments. Numerical simulations were also performed using a solver of the axisymmetric Euler equations. For the three surface conditions, close agreement between the measured and numerical waveforms was obtained, which shows that numerical simulations based on the Euler equations can accurately reproduce the effects of roughness on weak shock wave propagation.

In Qin and Attenborough [8], weak spherical shock waves were generated by focusing of a high-power laser beam. Their characteristics were similar to those obtained with a spark source. Several roughness values were considered with length scales between 0.2 and 5 mm. Microphones were used for the measurements of pressure waveforms, limiting their validity to the low-frequency range. Compared to the waveform for a smooth surface, a low-frequency component was noticed for the largest roughness scales and was identified as a surface wave. Surface waves above rough surfaces have been widely studied in the linear regime. Their existence is related to the property that a rough surface can be effectively replaced by a smooth surface with a frequency-dependent surface impedance [9,10]. The roughness causes an increase in, or creation of, the imaginary part of the effective impedance, thereby meeting one of the important conditions for the formation of a surface wave [9]. The amplitude of surface waves decays exponentially with height, but they undergo cylindrical spreading, rather than spherical spreading, with increasing distance from the source. At long range and grazing incidence, they can become a significant contribution to the pressure field. Since the 1970s, several experiments have been carried out to bring surface waves to light using as rough surfaces, either a lattice of rectangular cavities [11,12] or rectangular strips and cylinder arrays on a smooth surface [13,14], among others.

Experimental studies have been also performed using a shock tube and, consequently, for plane wave shocks. Though not directly applicable to spherical blast waves, they can give a hint as to the local reflection pattern [15]. In a series of papers, Ben-Dor, Takayama, and colleagues [16–18] considered the diffraction at a rough wedge and the transition from Mach reflection to regular reflection as the angle of the wedge increases. They observed that the transition angle was reduced due to roughness. For spherical blast waves, this implies that the Mach reflection should appear at a larger incidence angle for rough surfaces than for a smooth surface and, consequently, at a larger distance. Following Reichenbach [19], a detailed experiment on the diffraction of a shock with a Mach number of 1.425 at a crenellated wedge was performed by Adachi et al. [20]. Three angles of incidence, namely 20°, 30°, and 40°, were investigated. The crenellation had equal width and height, and six sizes (0.25, 0.5, 1, 2, 4, and 8 mm) were tested. A Mach stem was observed in all configurations, and two mechanisms for its formation were highlighted. The first mechanism was only observed for small angles of incidence (20° and 30°). As the plane shock impinges on the wedge, Mach reflection appears and a Mach stem grows as the plane shock propagates on the top of the first crenellation. The Mach stem then leaves it and continues growing in the crenellation cavity. As it impinges on the top of the second crenellation, a second reflected shock and Mach stem are observed at the foot of the first Mach stem. This pattern is repeated each time the plane shock impacts a new crenellation. A succession of triple points can thus be seen at the shock foot. At long distance, the reflected shocks merge into a single reflected shock, noted C_e. The second mechanism was observed for all the angles of incidence. As the plane shock propagates above the crenellation cavities, diffracted shock waves are generated. At a long distance, they also tend to merge into a single shock, noted C_{se}, which can be of sufficient amplitude to interact with the incident shock and form a Mach stem. In addition, in the cases for

which the two mechanisms were at play, the shock C_{se} was of larger amplitude than C_e and overtook it. Further analysis [21] revealed that the triple-point trajectory was discontinuous.

This paper aims at further studying the reflection of spherical weak blast waves over rough surfaces by performing a detailed numerical study. The objectives are to discuss the reflection pattern for rough surfaces and (if existing) to investigate some characteristics of the Mach stem observed experimentally, namely the reduction in its length, the delay in its formation compared to a smooth surface, and its absence for large roughness scales. In addition, the evolution of the peak pressure with the roughness scale is analyzed, with the aim of explaining the increase in peak pressure, observed in Karzova et al. [7].

The paper is structured as follows. In Sect. 2, the configuration, the numerical methods, and the source model are described. The reflection pattern for spherical weak shocks above a rough surface and its modification with source amplitude and roughness scale is examined in Sect. 3. The variations of the peak pressure along the surface, as well as the presence of a surface wave, are discussed in Sect. 4. Concluding remarks are given in Sect. 5.

2 Configuration and numerical model

2.1 Configuration

The propagation of a spherical blast wave above a rough surface is investigated. For simplicity, axisymmetric rough and flat surfaces are considered and the source is located on the axis of symmetry of the surface. The study can therefore be restricted to a two-dimensional (axisymmetric) problem. The cylindrical coordinates are denoted by (r, z). Similarly, for ease of analysis, the surface profile is chosen as sinusoidal:

$$\sigma(r) = \frac{h}{2}\cos\left(\pi\frac{r}{h}\right), \tag{1}$$

where h is the only roughness parameter. It can be interpreted as both the height and half-width of the asperities. In addition, the atmosphere is homogeneous and at rest and the air is assumed to be a perfect gas with the ratio of specific heats $\gamma = 1.4$. The geometry of the problem is sketched in Fig. 1.

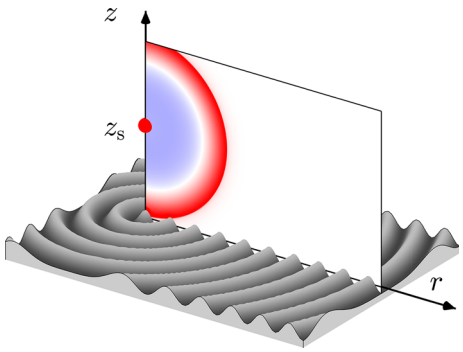

Fig. 1 Propagation of a spherical shock wave over a flat surface with axisymmetric roughness. An example of overpressure contours is shown

2.2 Equations and numerical methods

2.2.1 Equations

In what follows, ρ denotes the density, p the pressure, ρe the total energy density, u and w the radial and axial velocity components, respectively, and t the time. The variables are non-dimensionalized using the height of the source z_s as the length scale, the ambient density ρ_0 as the density scale, the ambient pressure p_0 as the pressure scale, the ambient sound speed $c_0 = \sqrt{\gamma p_0/\rho_0}$ as the velocity scale, and z_s/c_0 as the time scale.

The axisymmetric Euler equations are solved using high-order finite-difference techniques. To account for the rough surface, a body-fitted grid is used. A curvilinear coordinate transformation is then defined between the physical domain (r, z) and its computational counterpart (ξ, η). Using the notation $i_j = \partial i/\partial j$ for the metrics, the dimensionless equations are written in quasi-conservative form as:

$$\frac{\partial}{\partial t}\left(\frac{\mathbf{U}}{J}\right) + \frac{\partial}{\partial \xi}\left(\frac{\xi_r\mathbf{F} + \eta_r\mathbf{G}}{J}\right) + \frac{\partial}{\partial \eta}\left(\frac{\xi_z\mathbf{F} + \eta_z\mathbf{G}}{J}\right) + \frac{\mathbf{H}}{J} = 0, \tag{2}$$

where $\mathbf{U} = [\rho\ \rho u\ \rho w\ \rho e]^{\mathrm{T}}$ is the vector of the unknown variables, $J = \xi_r\eta_z - \xi_z\eta_r$ is the Jacobian of the transformation, and $\mathbf{F}$, $\mathbf{G}$, and $\mathbf{H}$ are vectors given by:

$$\mathbf{F} = \begin{bmatrix} \rho u \\ \rho u^2 + \frac{1}{\gamma}p \\ \rho u w \\ u(\rho e + p) \end{bmatrix} \quad \mathbf{G} = \begin{bmatrix} \rho w \\ \rho u w \\ \rho w^2 + \frac{1}{\gamma}p \\ w(\rho e + p) \end{bmatrix}$$

$$\mathbf{H} = \frac{1}{r}\begin{bmatrix} \rho u \\ \rho u^2 \\ \rho u w \\ u(\rho e + p) \end{bmatrix}. \tag{3}$$

These equations are complemented by the definition of the total energy density, which for a perfect gas writes:

$$\rho e = \frac{p}{\gamma - 1} + \frac{\gamma\rho}{2}\left(u^2 + w^2\right). \tag{4}$$

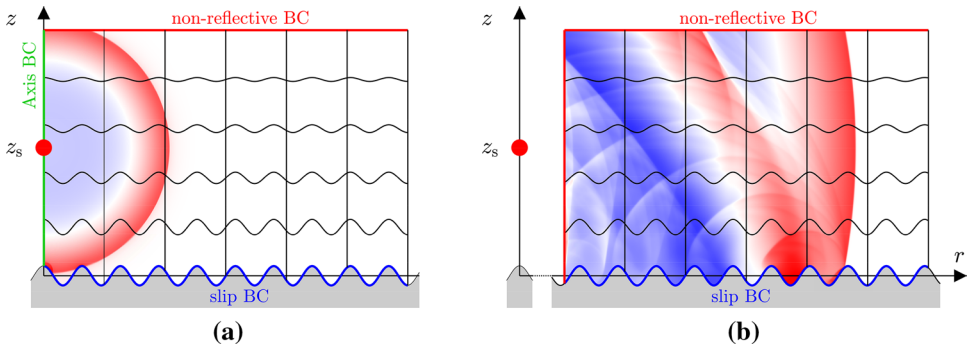

Fig. 2 Illustration of the computational domain with the boundary conditions **a** for a static frame and **b** for a moving frame. Examples of overpressure contours are shown

Note that the presence of the extra coefficient γ in (3) and (4) compared to the standard formulation of the Euler equations is due to the set of scales used.

The coordinate transformation proposed by Gal-Chen and Sommerville [22] is employed:

$$r(\xi, \eta) = \xi, \tag{5}$$

$$z(\xi, \eta) = \sigma(\xi) + \frac{\eta}{z_{\max}}[z_{\max} - \sigma(\xi)], \tag{6}$$

where $z_{\max}$ is the maximum height of the computational domain.

2.2.2 Numerical methods

As we consider the propagation of a signal of finite duration and thus of finite spatial extent, the useful information is contained near the incident and reflected shocks. It is thus not necessary to compute the shock propagation for a large domain in which the variables are mainly equal to their constant ambient values. To reduce the computational cost, the domain is thus restricted to a narrow domain that follows the propagation of the shocks. In detail, at each time step, we determine the last position along the r-direction at which the fluctuating pressure at the source height is greater than a threshold value (set to $p_s/10^4$). If this position is too close to the right boundary, the mesh is shifted along the r-direction by an integer number of mesh steps. This methodology, referred to as the moving frame [23], is illustrated in Fig. 2. It should be noted the moving frame usually employed for Cartesian grids can also be used for curvilinear grids, provided that a suitable coordinate transformation is adopted.

At the surface, a slip boundary condition is imposed by setting the normal wall velocity to zero. At the top boundary, the non-reflective boundary condition proposed by Bogey and Bailly [24] is used. At the left boundary, as long as the computational domain is static, axisymmetric boundary conditions as presented in Mohseni and Colonius [25] are used. More precisely, the symmetry of the variables is exploited to compute the spatial derivatives and to apply selective filtering using centered schemes along the ξ-direction. Note also that the $1/r$ singularity in the equations is treated by shifting the mesh in the ξ-direction by a half mesh size to avoid placing grid points at $r = 0$. Once the computational domain starts to move, non-reflective boundary conditions are applied at the left boundary instead of the axisymmetric boundary conditions.

Equation (2) is discretized by low-dispersion and low-dissipation explicit numerical schemes, developed in computational aeroacoustics. For the interior points, separated by at least five points from the boundary, and for the boundary points near the axis of symmetry, the centered fourth-order finite-difference scheme of Bogey and Bailly [26] and the centered sixth-order selective filter of Bogey et al. [27] are used. For the other boundary points, the 11-point non-centered finite-difference schemes and selective filters of Berland et al. [28] are implemented. To handle shock discontinuities, the shock-capturing methodology presented in Bogey et al. [27] with the detector proposed in Sabatini et al. [29] is applied. Time integration is carried out using a fourth-order six-stage Runge–Kutta algorithm [30].

The simulations are performed using an OpenMP-based in-house solver. The solver has been already used in two studies related to reflection of spherical weak shock waves over flat or rough surfaces [7,31]. An excellent agreement was obtained between the measured and simulated characteristics of the weak shocks, and in particular the overpressure waveforms. In addition, results of two test cases are presented in Supplementary Material of this article. The first test case deals with diffraction of a spherical pulse of small amplitude by a sphere. It aims to verify that diffraction by a curved surface is accurately simulated. The second test case considers plane-wave propagation of an N-wave. It aims to verify that nonlinear propagation of weak shocks is accurately simulated and does not generate spurious waves on a distorted mesh. Moreover, this solver was also employed in a related study to characterize the topographic effects on sonic boom reflection [32].

2.2.3 Computational parameters

The computational domain is $0 \leq \xi \leq 4.5$ and $0 \leq \eta \leq z_{\max} = 5$. The mesh is uniform, with a mesh size equal to 4×10^{-3} in the η-direction and to 1.5×10^{-3} for $0.01 \leq h \leq 0.045$ and 2.5×10^{-3} for $h = 0$ and $h \geq 0.05$ in the ξ-direction. This ensures that there are at least 13 points per period of the sinusoidal surface profile. A grid convergence study presented in Appendix 1 confirms that this choice of grid sizes allows for an accurate prediction of weak shock propagation over a rough surface. The mesh thus contains 2.25 or 3.75 million points, depending on the roughness. The time step is set to $\Delta t = 4.27 \times 10^{-4}$ and the corresponding CFL number is below 0.3 for all cases. The simulations are run using eight processors for 85,000 iterations, which allows for propagation distances up to $r = 36$.

2.3 Source and initial conditions

The source is set as an instantaneous release of energy with a Gaussian spatial envelope via the initial conditions:

$$p(r, z, t = 0) = 1 + p_s \exp\left(-\log(2)\frac{r^2 + (z-1)^2}{B^2}\right), \tag{7}$$

$$\rho(r, z, t = 0) = 1, \tag{8}$$

$$\rho u(r, z, t = 0) = 0, \tag{9}$$

$$\rho w(r, z, t = 0) = 0. \tag{10}$$

This source model has previously been employed for the study of spherical weak shock wave propagation above a flat and smooth surface [31] and was shown to produce pressure waveforms similar to those measured for an electric spark source. The source is characterized by its width B and its maximal overpressure p_s. Unless otherwise stated, they are set to $B = 0.25$ and $p_s = 7.5$. An important parameter for spherical shock wave is the source energy E_s, which is the main factor for the positive phase of the pressure waveform. It is obtained by integrating the energy density over the source volume, which relates E_s, $B_s = B/\sqrt{\log(2)}$, and p_s with:

$$E_s = \frac{p_s}{\gamma - 1}\pi^{3/2} B_s^3. \tag{11}$$

A preliminary simulation is performed in free field to get the characteristics of the incident shock wave on the surface. Figure 3a shows the evolution of the Mach number along the surface. The shock velocity was determined from the pressure jump at the shock and the Rankine–Hugoniot relation. The Mach number of the incident spherical shock does not exceed 1.3, it is smaller than 1.05 from $r > 3.3$, and it reaches 1.003 at $r = 35$. As an example, the time series of the overpressure

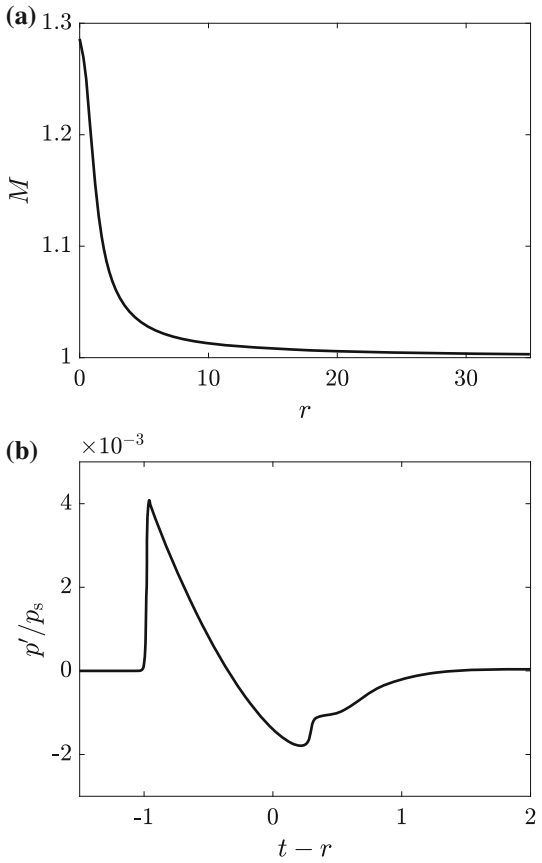

Fig. 3 **a** Mach number of the incident shock wave on the surface as a function of the radial coordinate. **b** Example of an overpressure waveform in free field at $r = 10$

$p' = p - 1$ in free field at $r = 10$ is depicted in Fig. 3b. Notice that the shape of the waveform generated by the source is typical of a blast wave.

2.4 Discussion of the non-dimensionalization

The parameters of the source and of the rough surface have been chosen to correspond to the measurements at laboratory scale of Karzova et al. [7]. The height of the spark source was about $z_s = 1$ cm with propagation distances up to $r = 33$ cm. In the model for the spark source [31], the maximal overpressure is $p_s = 7.5 \times 10^5$ Pa and the source characteristic length is $B = 0.25$ cm, which yields a source energy of $E_s = 0.28$ J. Assuming that a gram of TNT represents 4610 J [1], this source is equivalent to a mass of 61.3 µg of TNT. The roughness scales considered in the paper are between 100 and 1500 µm, which are in the order of the roughness correlation lengths for the sandpapers used in Karzova et al. [7].

For a source height of $z_s = 1$ m with the same ratio B/z_s and the same source amplitude, the results shown in the paper correspond to a source with an energy of 283.7 kJ or to an

equivalent mass of TNT of 61.3 g and to roughness scales between 1 and 15 cm.

3 Reflection pattern

3.1 General comments

In order to investigate the effect of roughness on the reflection pattern, schlieren pictures are shown at several instants in time in Fig. 4 for three different surface conditions. They are obtained by calculating the norm of the density gradient $|\nabla\rho|$ and allow for a clear visualization of the shocks. At $t = 0.43$, the spherical incident shock impinges the surface. At $t = 0.85$, a single reflected shock, which intersects the incident shock on the surface, is observed for the smooth surface, while additional diffracted shocks at the surface asperities can be seen for the rough surfaces. At $t = 1.71$, the reflection pattern for the smooth surface is of Mach type: There are three shocks with different slopes at the triple point. For the rough surfaces, a contribution is predominant over all the diffracted shocks and can be interpreted as an effective reflected shock. At following times, the Mach stem grows for the smooth surface and the reflection pattern progressively switches from Mach reflection to von Neumann reflection, as the shock front of the incident shock and of the Mach stem becomes continuous along the triple point. For the rough surface $h = 0.02$, the effective reflected shock has caught up and merged with the incident shock by $t = 3.42$. As for a smooth surface, the Mach stem then grows at following times. For $h = 0.05$, the effective reflected shock progressively catches up with the incident shock at $t = 3.42$ and 7.26 before merging at $t = 13.2$.

Additional close-up schlieren pictures near the surface for $h = 0.05$ are shown in Fig. 5 to clarify the reflection pattern for the rough surface. A schematic drawing is depicted in Fig. 6 to facilitate the discussion. The incident spherical shock (I) is observed at $t = 0.42$. Once it has impinged on the surface, diffracted waves are generated first, at the top of the asperities, at $t = 0.46$. The majority of the energy is diffracted leftward, and the amplitude of diffracted waves propagating along with the incident shock wave is comparatively small. As the incident shock continues to propagate in the surface cavities, a reflection pattern similar to a triple-shock pattern is observed at its foot (at $t = 0.55$, 0.59, 0.67, or 1.05). However, the amplitude of the diffracted wave is expected to be too small to interact nonlinearly with the incident shock. Once the incident shock reaches the bottom of the cavity, other diffracted waves are generated and propagate upward, as seen for $t = 0.5$. As they propagate, the different diffracted waves progressively coalesce into two wavefronts ($t > 0.55$). The first one (R_t), corresponding to the waves diffracted at the top of the asperities, is attached to the incident shock. The second one (R_b), of larger amplitude, corresponding to the waves diffracted at the bottom of the asperities, is detached from the incident shock. At long range, the latter becomes the effective reflected wave, shown in Fig. 4, that may interact with the incident shock. From the schlieren picture at $t = 1.26$, it is noted that the space between the incident and reflected shocks near the surface and close to the source is of the order of the roughness period $2h$. In addition, a fourth wavefront (D) can be seen at $t = 0.84$, 1.05, and 1.26 and is due to diffracted waves that are diffracted a second time at the surface asperities.

3.2 Effect of the source amplitude

Figure 7 shows schlieren pictures at time $t = 19.1$ for three surface conditions and five source amplitudes. For $p_s = 0.01$, the source amplitude is sufficiently small for the propagation to be essentially linear and there is no shock. The pictures for the smooth surface and the rough surface with $h = 0.02$ have similar patterns. For $h = 0.05$, additional contributions can be distinguished near the surface for $r < 18.5$. For the smooth surface, the Mach reflection is observed from $p_s = 1$. As the source amplitude increases, the Mach stem grows. With the rough surfaces, the incident and reflected shocks first appear separated. The space between them reduces with increasing p_s, and the Mach stem is formed starting from $p_s = 4$ for $h = 0.02$ and $p_s = 8$ for $h = 0.05$. Moreover, the contributions observed near the surface for $h = 0.05$ and $p_s = 0.01$ are observed for $p_s \geq 1$ just behind the reflected shock. A similar pattern can also be identified for $h = 0.02$ and $p_s \geq 1$.

The trajectory of the triple point for these three surface conditions is now investigated for different source amplitudes. It is determined graphically from the schlieren pictures. The triple-point location is accurately estimated when the slopes of the three shocks at the triple point differ significantly. However, at long range, these slopes have comparable values, which makes the determination of the triple-point location imprecise. In this case, the estimated precision for the triple-point location is ± 0.1. In addition, for a rough surface, the merging of the incident and reflected shocks can occur at a long distance from the source, at which point the propagation direction and the speed of the incident and reflected shock fronts are almost identical. The incident and reflected shocks thus appear on the schlieren pictures as two parallel lines that slowly come closer, and the exact instant at which the Mach stem appears is then difficult to determine. In the following, only the location of triple points that can be clearly distinguished in the schlieren pictures is reported, so that the starting point of the triple-point trajectory for rough surfaces can not only be on the surface but above.

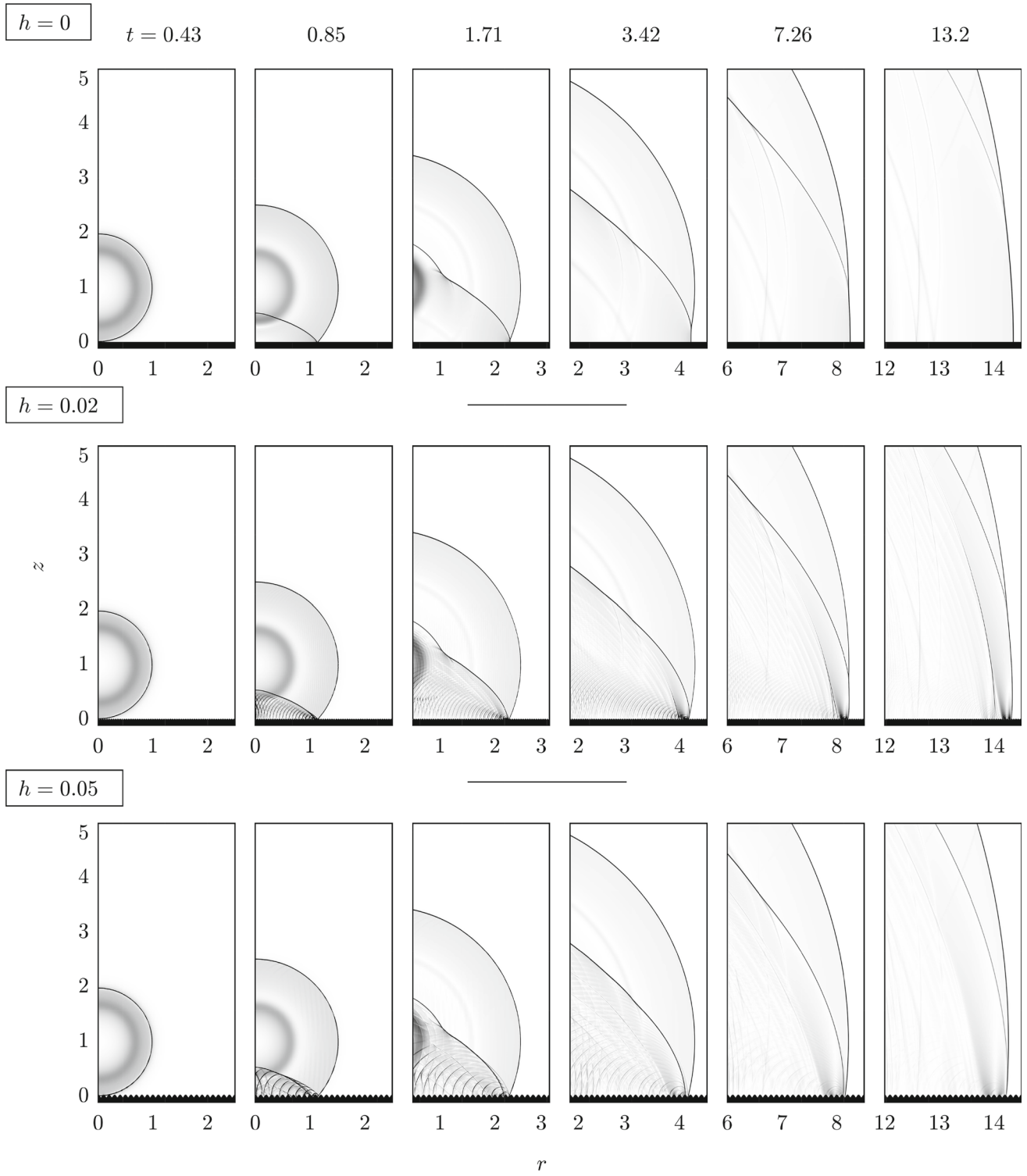

Fig. 4 Schlieren pictures showing the time evolution of the reflection pattern at $t = 0.43$, 0.85, 1.71, 3.42, 7.26, and 13.2 and for surfaces with (top) $h = 0$, (middle) 0.02, and (bottom) 0.05. The source amplitude is $p_s = 7.5$

The triple-point trajectory for the smooth surface and for several source amplitudes is shown in Fig. 8a. As reported for blast waves [1,6,33] and noticed previously for similar simulations [31], the trajectory has a parabolic shape. The source amplitude is a key parameter to estimate this trajectory. As it increases, the triple point leaves the wall closer

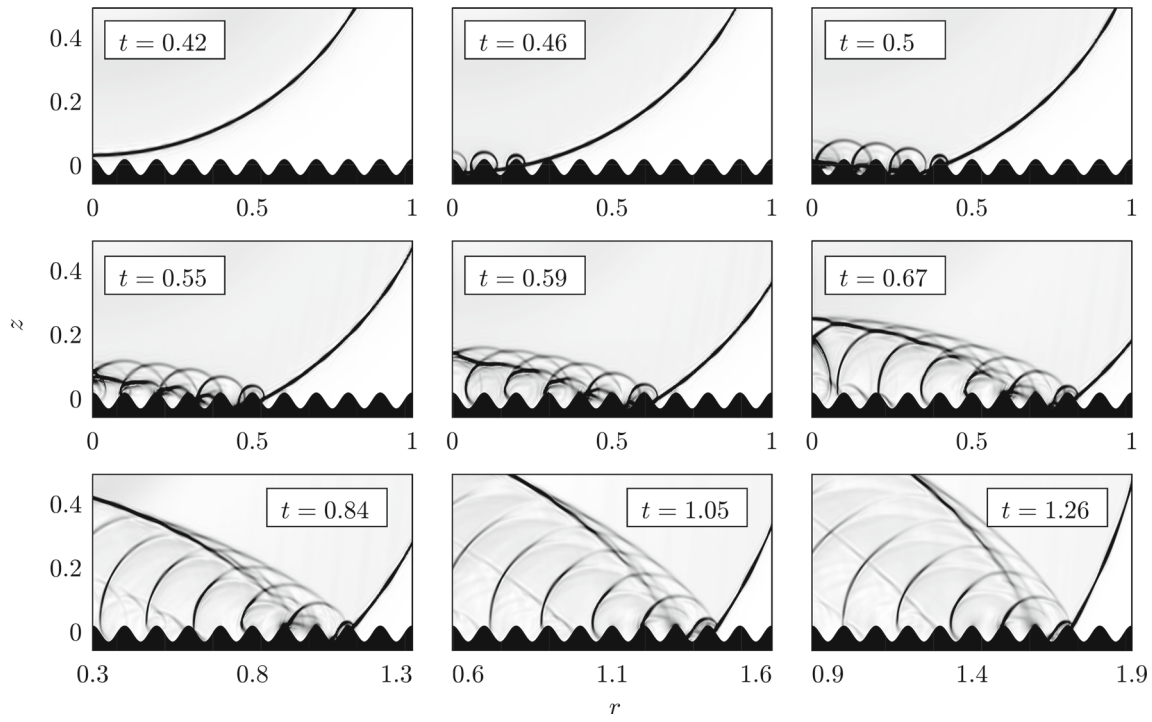

Fig. 5 Close-up schlieren pictures for $h = 0.05$ and for $t = 0.42$, 0.46, 0.5, 0.55, 0.59, 0.67, 0.84, 1.05, and 1.26

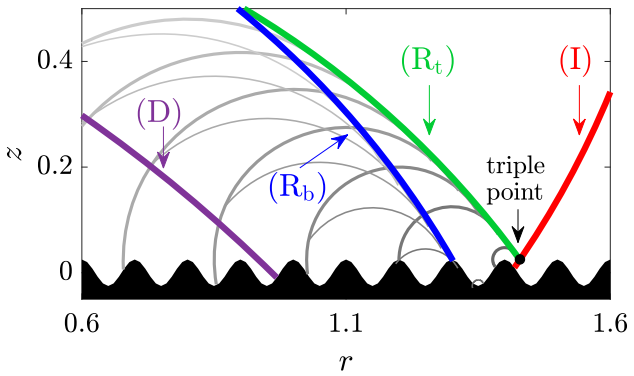

Fig. 6 Schematic diagram representing the reflection pattern for a rough periodic surface observed in Fig. 5

to the source and its vertical velocity increases as well. For comparison purposes, Fig. 8b, c shows the trajectory of the triple point for the two rough surfaces with $h = 0.02$ and $h = 0.05$, respectively. Contrary to the smooth surface, there is no Mach stem for $p_s = 1$ and $h = 0.02$. For $h = 0.05$, the Mach reflection is only observed for $p_s = 6$, 7, and 8. It is also noticed that the roughness induces a delay in the formation of the Mach stem. Thus, for $p_s = 4$, the triple point can be observed from $r = 3.1$ for the smooth surface but from $r = 6.2$ for the rough surface $h = 0.02$. Once formed, the growth of the Mach stem follows a similar evolution than for a smooth surface. As discussed by Dewey et al. [3], the reflection pattern for a rough surface at long range is equivalent to the one with a smooth surface and a smaller energy source at a closer distance. For instance, the trajectory of the triple point for a smooth surface and for a source amplitude $p_s = 3$ is comparable to the one for a rough surface $h = 0.02$ with a source that is more energetic, $p_s = 5$, and a delay in the apparition of the Mach stem $\Delta r = 1$. For the larger roughness scale $h = 0.05$, the source amplitude should be increased to $p_s = 8$ and the delay to $\Delta r = 5.5$.

3.3 Effect of the roughness scale

Figure 9 shows schlieren pictures at $t = 19.1$ for several roughness scales and for a source amplitude $p_s = 7.5$. Mach reflection is observed for $h \leq 0.05$. The Mach stem gradually shortens with h. For the largest roughness scales $h = 0.1$ and 0.15, the incident and reflected shocks are detached. This echoes the measurements of Karzova et al. [7] using sandpapers in which the Mach stem was observed for the smaller grain and was absent for the larger one. For h between 0.015 and 0.04, a fourth shock is observed behind the triple-shock pattern. It is related to the double-diffracted waves noticed in Fig. 5 and referred to as (D) in Fig. 6. Finally, for all the roughness cases, the contribution located near the surface and attached to the incident shock is observed. Its wavelength appears to vary with the roughness scale.

The triple-point trajectories for the smooth surface and rough surfaces for which $h \leq 0.06$ are shown in Fig. 10. As observed in outdoor or laboratory experiments [3,5,7], it is

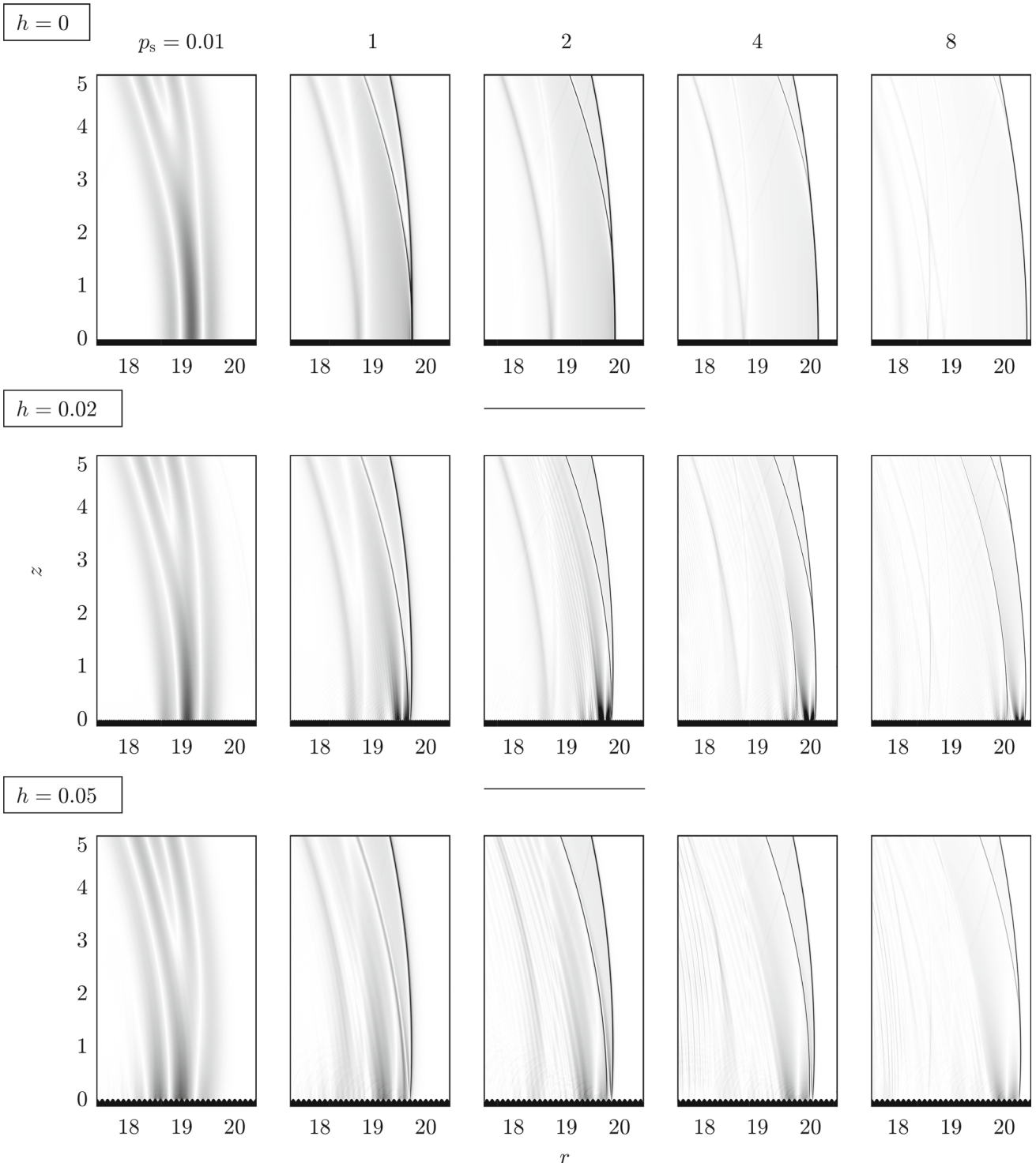

Fig. 7 Schlieren pictures at $t = 19.1$ for (top) $h = 0$, (middle) 0.02, and (bottom) 0.05 and for five source amplitudes $p_s = 0.01$, 1, 2, 4, and 8

found that, for a given distance, the length of the Mach stem reduces with the roughness scale. In addition, the delay in the formation of the triple point is seen to increase with h. Finally, once formed, the height of the Mach stem increases less rapidly with the roughness scale. For instance, it grows from $z_M = 1$ to 2 over a distance of $\Delta r = 4$ for $h = 0$ but over a distance of $\Delta r = 4.4$ for $h = 0.02$ and $\Delta r = 6$ for $h = 0.05$.

This delay in the formation of the triple point for a rough surface can be attributed to two factors. First, the roughness

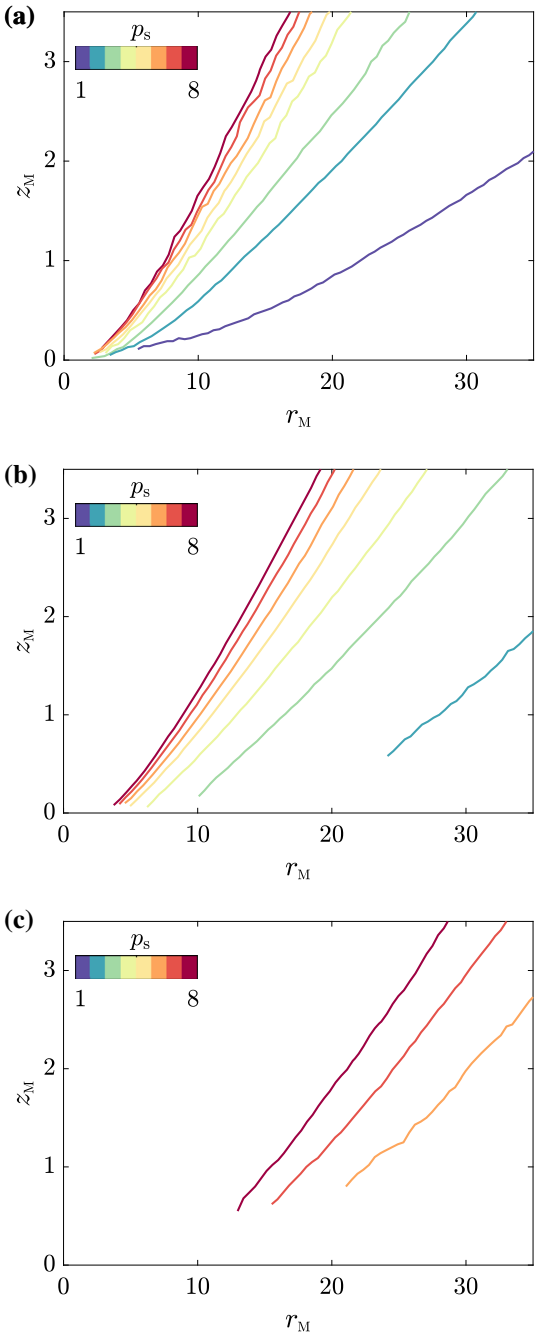

Fig. 8 Trajectory of the triple point **a** for a smooth surface and for a rough surface with **b** $h = 0.02$ and **c** $h = 0.05$ and for different source amplitudes

induces a delay in the formation of the effective reflected shock, because it originates from the merging of the waves diffracted at the bottom of the surface asperities as seen from the close-up schlieren pictures in Fig. 5. Second, the amplitude of the effective reflected shock decreases with the roughness, which tends to reduce the nonlinear interaction between the direct and reflected shocks. These two points are illustrated in Fig. 11, which shows the overpressure waveforms at $r = 5$ and $z = 1$ for $h \leq 0.1$. At this location, the Mach stem is not yet formed for any of the surfaces considered, and the direct and reflected shocks are separated. The direct shock is first observed at the reduced time $t - r = -0.9$ and is the same for all the surfaces. The reflected shock is then seen, starting from $t - r = -0.7$ for the smooth surface. It is noticed that the arrival time of the effective reflected shock increases with the roughness, while its amplitude reduces.

4 Overpressure

4.1 Profiles of peak overpressure

The evolution of the maximum value of the pressure along the surface is now considered. For the rough surfaces, it presents a periodic behavior associated with roughness periodicity, with local minima and maxima, as suggested in Fig. 5, for instance. For better readability, a moving average is applied over three periods of the rough profile to smooth the curves.

The evolution of the peak pressure along the surface for both the smooth and rough surfaces is shown in Fig. 12a. As expected, the peak pressure diminishes with range for the smooth surface. A slower decrease is observed near $r = 5$, where the Mach stem is forming. The peak pressure on the surface decreases with roughness scale. However, for $h \leq 0.1$, it is greater than with the smooth surface over the entire range considered. The opposite behavior is only observed for the largest roughness scales and at long range ($r \geq 10$). In order to extrapolate the overpressure decay at larger distances, the curves are fitted by the power law $\max(p') \propto r^{\alpha}$ over the range $20 \leq r \leq 35$. The resulting values of α are plotted as a function of h in Fig. 12b. For the smooth surface, it is equal to $\alpha = -1.23$, which is close to the expected value for spherical shock waves in free field [34]. For rough surfaces, α is smaller than with the smooth surface for $h < 0.04$, which means that at longer range the peak pressure for the smooth surface will be greater. The opposite behavior is observed for $h \geq 0.04$, implying that, in particular, the peak pressure for $0.05 \leq h \leq 0.1$ will remain larger for rough surfaces at increased distances.

Figure 13 shows the vertical profile of the peak overpressure at $r = 30$. In accordance with Fig. 12, the peak overpressure at the surface ($z = 0$) is greater for rough surfaces with $h < 0.1$ than for the smooth surface. Near the surface, the peak overpressure decreases exponentially with height for rough surfaces. In contrast, it is almost constant along the Mach stem for a smooth surface. Above the surface ($z \geq 2$), the peak overpressure is comparable to that of a smooth surface for the smallest roughness scales ($h < 0.04$) and then gradually decreases with h to attain a constant value, which corresponds to the peak overpressure value in free field.

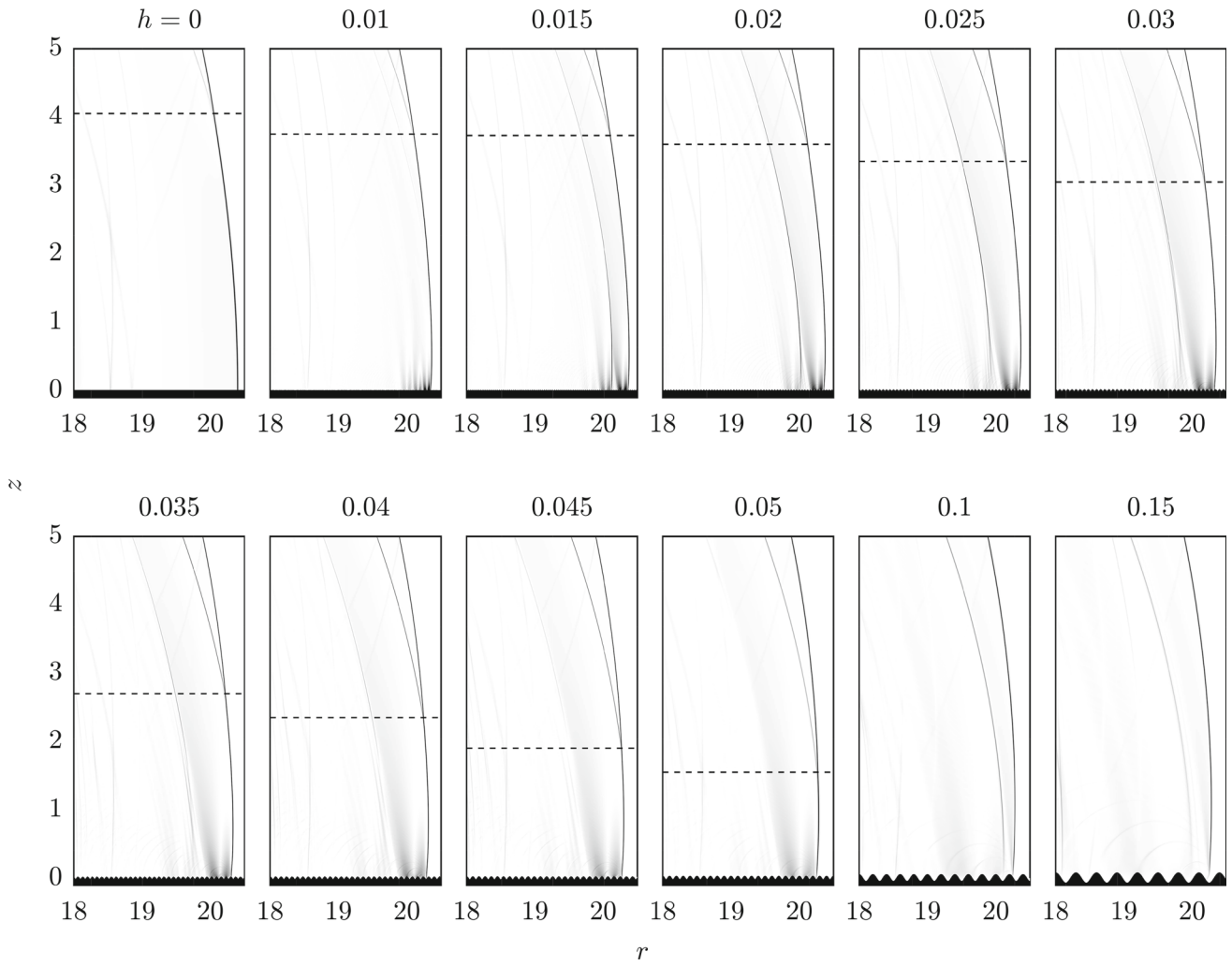

Fig. 9 Schlieren pictures showing the reflection pattern at $t = 19.1$ for several roughness scales with the same source amplitude, $p_s = 7.5$. The height of the triple point is indicated by a dashed line

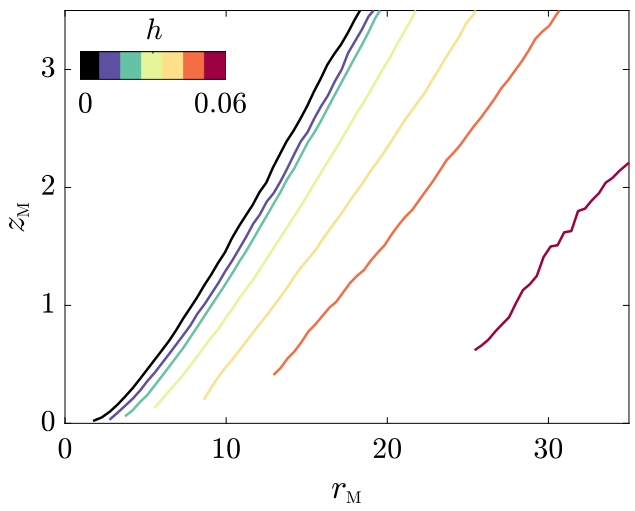

Fig. 10 Trajectory of the triple point for different surface conditions with the same source amplitude, $p_s = 7.5$

The overpressure waveforms for the smooth surface and some rough surfaces at long range $r = 30$ and just above the surface at $z = 0.2$ are depicted in Fig. 14. The waveform for a smooth surface looks like a blast wave in free field, with the peak overpressure at the shock discontinuity (see also Fig. 3b). Roughness has a dramatic effect on the waveform. First, the shock strength decreases with roughness scale. Second, an oscillation appears after the shock. Its period is related to the roughness scale, as it tends to increase with h. In addition, its maximum value is greater than the pressure at the shock front. For small roughness scales, it is even greater than the peak overpressure for a smooth surface. In addition, note that the waveforms for the large roughness scales are similar to the one reported in Fig. 11 in Qin and Attenborough [8]. In particular, the low-frequency oscillation was associated with the presence of a surface wave.

Figure 15 shows the peak overpressure and the shock pressure jump determined from the waveforms in Fig. 14 as a

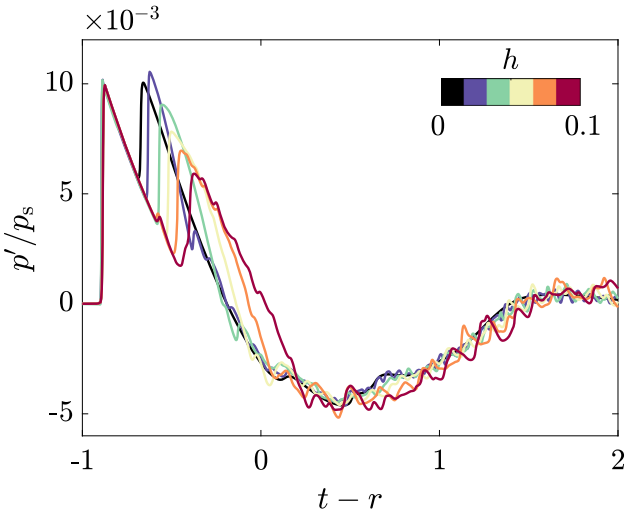

Fig. 11 Overpressure waveforms at $r = 5$ and $z = 1$ for different surface conditions

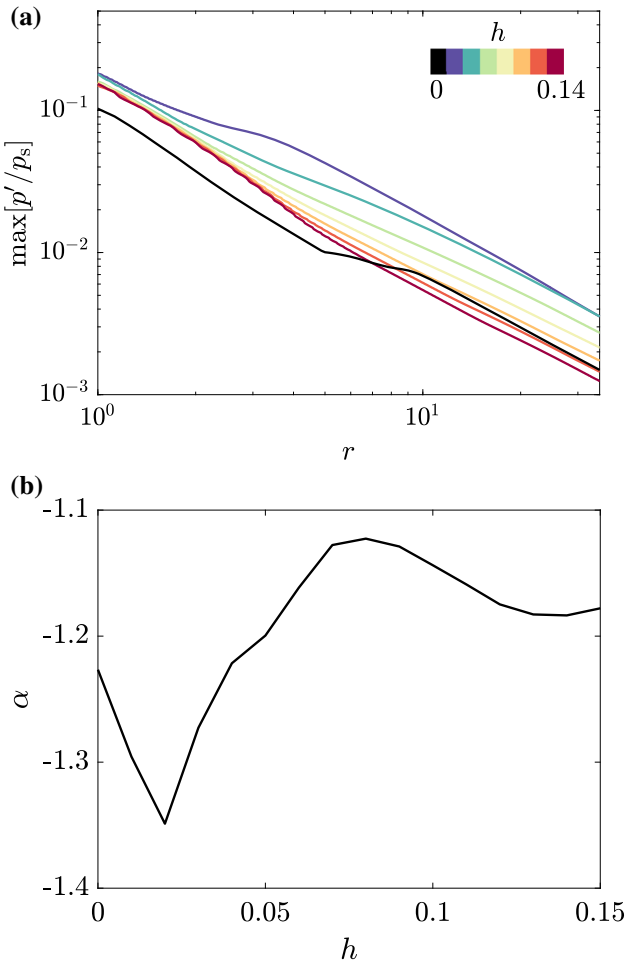

Fig. 12 **a** Evolution of the peak overpressure $\max(p')$ along the surface for the smooth and the rough surfaces. **b** Coefficient α of the fit $\max(p') \propto r^{\alpha}$ over the range $20 \leq r \leq 35$ as a function of roughness scale

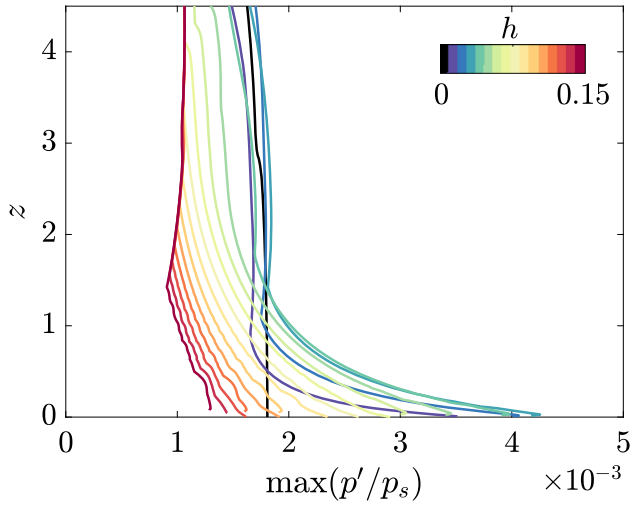

Fig. 13 Vertical profile of the peak overpressure at $r = 30$ for different surface conditions

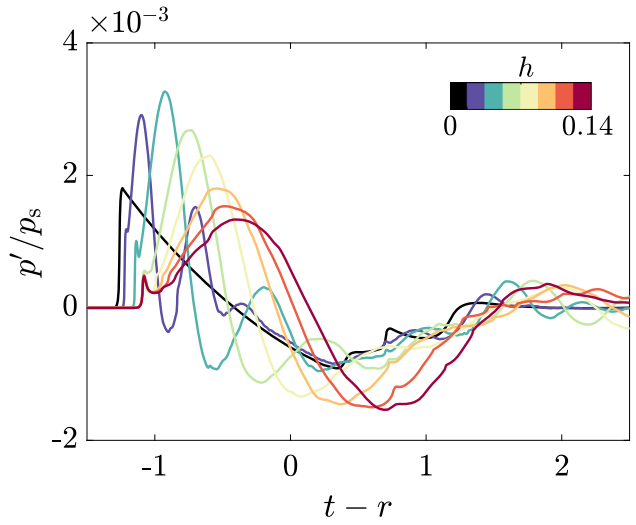

Fig. 14 Overpressure waveforms at $r = 30$ and $z = 0.2$ for different surface conditions

function of h. It is observed that the maximum overpressure first increases up to $h = 0.03$ before decreasing. At its maximum, the peak overpressure is one and a half times greater than for a smooth surface. The shock pressure jump reduces with h and becomes almost constant for $h > 0.07$. Compared to a smooth surface, it diminishes at most by a factor of 4. This could explain differences between experimental studies regarding the peak overpressure: In Dewey et al. [3] and Huber and McFarland [5], roughness was noticed to induce a reduction in peak overpressure, but, on the contrary, Karzova et al. [7] observed an increase in peak overpressure. While peak overpressure was determined directly from the waveforms in Karzova et al. [7], they were calculated from the shock speed in Dewey et al. [3] and Huber and McFar-

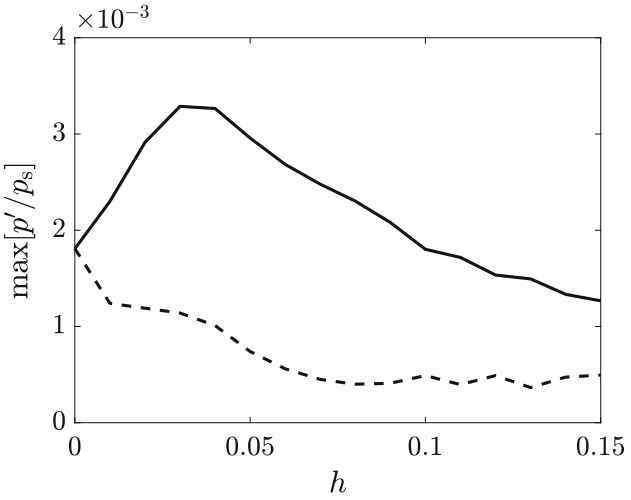

Fig. 15 (Solid) Peak overpressure and (dashed) shock pressure jump at $r = 30$ and $z = 0.2$ as a function of h

land [5]. This corresponds to the shock overpressure, which is actually smaller for rough surfaces than for a smooth surface.

4.2 Surface wave

The characteristics of the pressure near the surface at long range, namely the exponential decay of the amplitude with height and the presence of oscillations on the waveforms, evoke the presence of a surface wave. This section aims at confirming this point and at examining the variations of the surface wave with roughness scale and source amplitude.

4.2.1 Comparison in the linear regime

In order to confirm the oscillations observed on the waveforms are due to a surface wave, the numerical solution is compared with an analytical solution in the linear regime, in which the surface wave contribution is explicit.

In the linear regime ($p_s \ll 1$), the initial value problem becomes:

$$\frac{\partial^2 p'}{\partial t^2} - \Delta p' = 0, \tag{12}$$

$$p'(r, z, t = 0) = p_s \exp\left(-\log(2)\frac{r^2 + (z-1)^2}{B^2}\right), \tag{13}$$

$$\frac{\partial p'}{\partial t}(r, z, t = 0) = 0, \tag{14}$$

with the slip boundary condition at the rough surface:

$$\frac{\partial p'}{\partial n}(r, z = \sigma(r), t) = 0, \tag{15}$$

where $\partial/\partial n$ is the normal derivative.

Analytical solutions for this kind of initial value problem can be formulated based on the Green's function of the associated Helmholtz equation. Indeed, the initial conditions in (13)–(14) lead to the propagation of a pulse with a spherical symmetry, as if generated by a broadband point source. The spectrum of this equivalent point source can be shown to depend on the spatial Fourier transform of the pulse distribution [35]. For that, the Fourier transform of the overpressure:

$$p'(r, z, t) = \frac{1}{2\pi}\int_{-\infty}^{+\infty} \hat{p}(r, z, \omega)\mathrm{e}^{-\mathrm{i}\omega t}\mathrm{d}\omega, \tag{16}$$

is first introduced. In the above equation, ω denotes the angular frequency and is related to the frequency $f = \omega/(2\pi)$. It is recalled that the frequency, like the other variables, is dimensionless and that the frequency scale is c_0/z_s in accordance with the set of scales proposed in Sect. 2.2.1. The problem in (12)–(14) is then equivalent to:

$$\Delta\hat{p} + \omega^2\hat{p} = S(\omega)\frac{\delta(r)}{\pi r}\delta(z-1), \tag{17}$$

with the source spectrum:

$$S(\omega) = p_s \mathrm{i}\omega\pi^{3/2}B_s^3 \exp\left(-\frac{\omega^2 B_s^2}{4}\right). \tag{18}$$

Before going further, the smoothed boundary condition approach is introduced with the aim of formulating an analytical solution to the problem. It consists in replacing the slip boundary condition on the rough surface $z = \sigma(r)$ by an admittance boundary condition on the smoothed surface $z = 0$:

$$\frac{\partial\hat{p}}{\partial z}(r, z = 0, \omega) + \mathrm{i}\omega\beta\,\hat{p}(r, z = 0, \omega) = 0, \tag{19}$$

with an admittance β that depends on the frequency, the geometry, and the roughness characteristics. For a 1D rough surface made of the sinusoidal profile introduced in (1), the effective admittance is given by the boss model [9,36] at grazing incidence and at low frequencies ($\omega h \leq 1$) by:

$$\beta(\omega) = -\mathrm{i}\omega\alpha h, \tag{20}$$

with $\alpha \approx 0.2$. Details on the derivation are given in Appendix 2.

The analytical solution of (17) with the boundary condition in (19) can be written as a sum of three contributions: [37]

$$\hat{p}(r, z, \omega) = \hat{p}_{\mathrm{DW}}(r, z, \omega) + \hat{p}_{\mathrm{RW}}(r, z, \omega) + \hat{p}_{\mathrm{SW}}(r, z, \omega). \tag{21}$$

The first one is the direct wave:

$$\hat{p}_{\mathrm{DW}}(r,z,\omega) = -S(\omega)\frac{\exp(\mathrm{i}\omega R_1)}{4\pi R_1}, \tag{22}$$

with $R_1 = \sqrt{r^2+(z-1)^2}$ being the distance between the source and the receiver. The second contribution can be interpreted as the reflected wave and is given for $\mathrm{Im}(\beta) < 0$ by:

$$\hat{p}_{\mathrm{RW}}(r,z,\omega) = -S(\omega)\left[\frac{\exp(\mathrm{i}\omega R_2)}{4\pi R_2} -2\mathrm{i}\omega\beta\int_{-\infty}^{0}\exp(\mathrm{i}\omega\beta q)\frac{\exp(\mathrm{i}\omega R_q)}{4\pi R_q}\mathrm{d}q\right], \tag{23}$$

with $R_2 = \sqrt{r^2+(z+1)^2}$ being the distance between the image source and the receiver and $R_q = \sqrt{r^2+(z+1+q)^2}$. Finally, the third contribution is the surface wave:

$$\hat{p}_{\mathrm{SW}}(r,z,\omega) = S(\omega)\frac{\omega\beta}{2} \times \exp[-\mathrm{i}\omega\beta(z+1)]H_0^{(1)}\left(\sqrt{1-\beta^2}\omega r\right), \tag{24}$$

with $H_0^{(1)}$ being the Hankel function of the first kind and of zeroth order. It is noticed that the surface wave amplitude decays inversely as the square root of the propagation distance and exponentially with height, with a skin depth $1/|\omega\,\mathrm{Im}(\beta)|$. The analytical solution for each of the contributions in the time domain can then be calculated from the Fourier transform in (16).

Comparisons between the numerical and analytical solutions for a source amplitude $p_\mathrm{s} = 0.01$ and for two rough surfaces with $h = 0.02$ and 0.05 at $r = 30$ and $z = 0.2$ are shown in Fig. 16. The contribution of the surface wave component is also represented. The agreement between the numerical and analytical solutions is satisfactory, especially for the smallest roughness. It is noted that the oscillations at the tail of the waveform for $h = 0.05$ are reproduced by the analytical solution, although they are of reduced amplitude and period. As expected, these are due to the surface wave component. In fact, the entire waveform for $h = 0.05$ is due almost exclusively to the surface wave. The discrepancies between the numerical and analytical solutions for $h = 0.05$ may be due to the low-frequency assumption for determining the effective admittance (i.e., $\omega h \leq 1$), which starts to be restrictive for this roughness scale: The period of oscillations for the surface wave component is thus about 0.6, corresponding to an angular frequency of $0.5/h$.

4.2.2 Effect of the roughness scale

The variation of the surface wave characteristics with the roughness scale is investigated. Information is first obtained

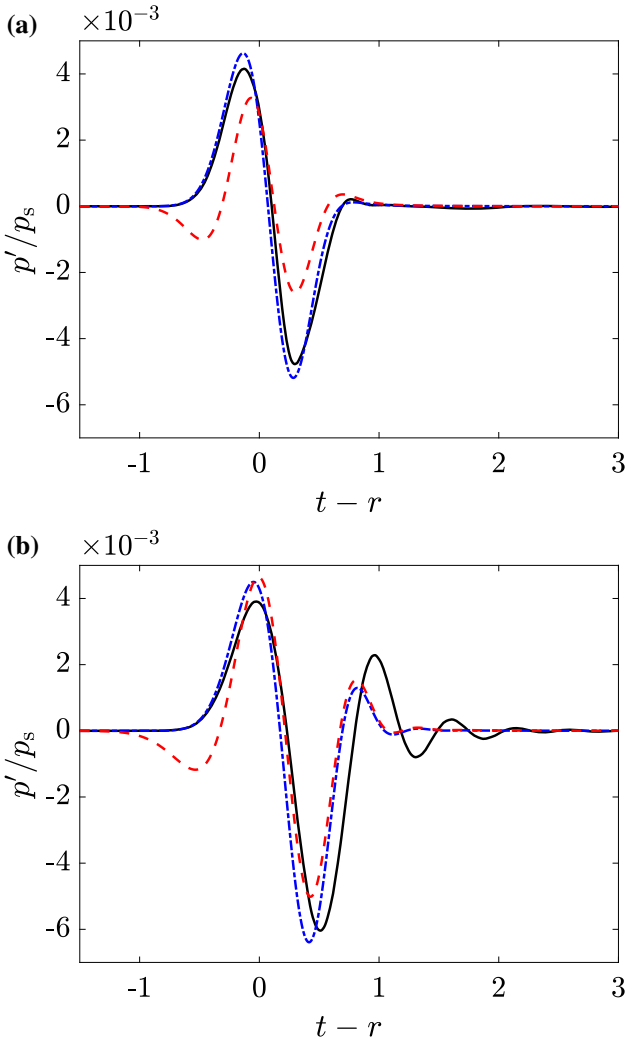

Fig. 16 Waveforms of the overpressure for $p_\mathrm{s} = 0.01$ at $r = 30$ and $z = 0.2$ for two rough surfaces with **a** $h = 0.02$ and **b** $h = 0.05$: (solid) numerical solution, (dash-dotted) analytical solution, and (dashed) surface wave component

in the linear regime from the analytical expression in (24). In the frequency range of interest, $\omega h \ll 1$, one has $|\beta| \ll 1$ and $\sqrt{1-\beta^2} \approx 1$. Approximating $|H_0^{(1)}(u)| \approx \sqrt{2/(\pi u)}$, the modulus of the surface wave component is then expressed as:

$$|\hat{p}_{\mathrm{SW}}(r,z,\omega)| = p_\mathrm{s}\,\omega^{5/2}\alpha h B_\mathrm{s}^3\frac{\pi}{\sqrt{2r}} \times \exp\left[-\omega^2\left(\frac{B_\mathrm{s}^2}{4}+\alpha h(z+1)\right)\right]. \tag{25}$$

The maximum of $|\hat{p}_{\mathrm{SW}}|$ is thus obtained at the frequency f_{SW}:

$$f_{\mathrm{SW}} = \frac{1}{2\pi}\left(\frac{5}{4\alpha h(z+1)+B_\mathrm{s}^2}\right)^{1/2}. \tag{26}$$

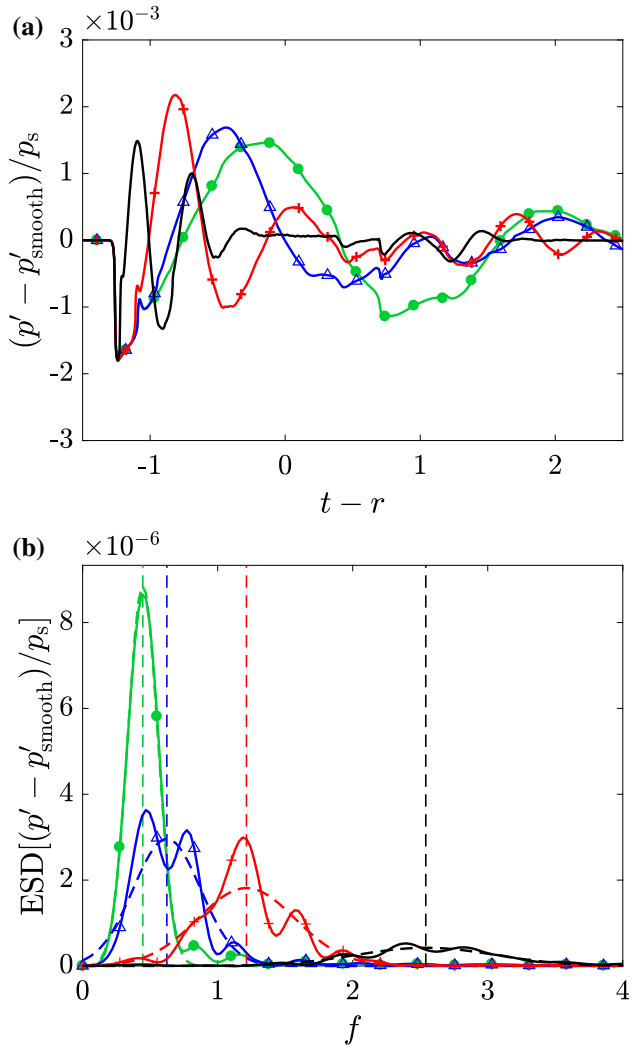

Fig. 17 **a** Signal obtained by subtracting the waveform for the smooth surface to the one for a rough surface at the same position $r = 30$ and $z = 0.2$ and **b** corresponding energy spectral densities: (solid) $h = 0.02$, (cross) $h = 0.05$, (triangle) $h = 0.1$, and (circle) $h = 0.15$. The vertical lines in (**b**) indicate the central frequency f_{SW} of the surface wave hump. The source amplitude is $p_{\mathrm{s}} = 7.5$

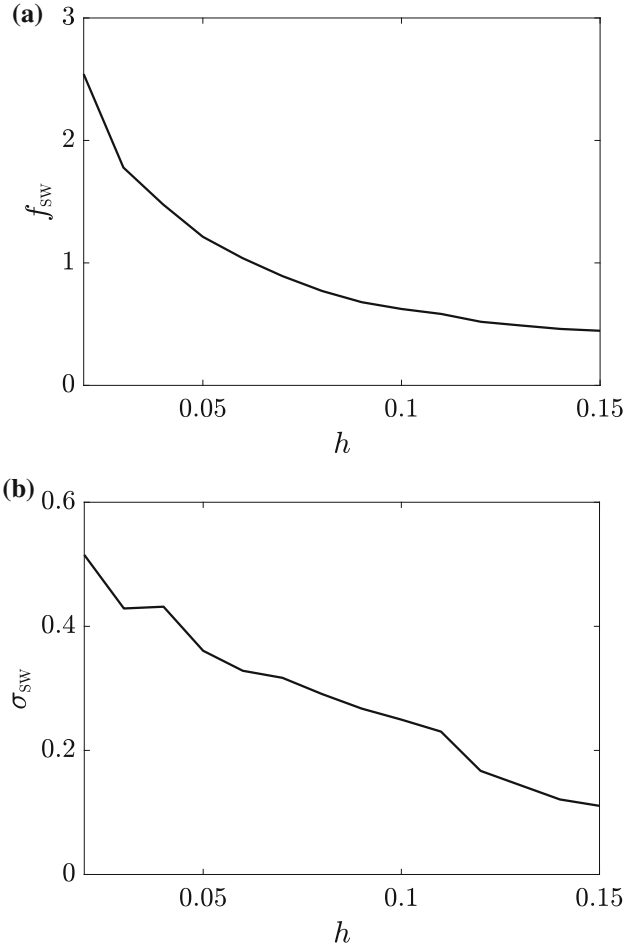

Fig. 18 Estimated **a** central frequency and **b** half-width of the surface wave spectrum as a function of the roughness scale h for $p_{\mathrm{s}} = 7.5$

It depends on the roughness scale and also on the frequency content of the pulse through the parameter B_{s}. As B_{s} is notably greater than h, f_{SW} is slightly dependent on h. For instance, it is equal to 1.08 for $h = 0.02$ and 0.96 for $h = 0.05$.

For higher values of p_{s}, information about the surface wave has to be extracted from the numerical solution. To do so, the oscillations due to the surface waves are separated from the rest of the waveform by examining the difference between the waveforms corresponding to the rough and smooth surfaces. An example of the resulting signal is shown in Fig. 17a for four values of h. While the shock discontinuities at the start of the signal are not eliminated by this procedure, the oscillations are clearly visible and they have most energy. The corresponding one-sided energy spectral densities ($\mathrm{ESD}[p](f) = 2|\hat{p}(f)|^2$) are depicted in Fig. 17b. They present a hump whose central frequency and bandwidth decrease with h. To quantitatively analyze this hump, the energy spectral densities are fitted by a Gaussian function:

$$A_{\mathrm{SW}} \exp\left[-\log(2) \frac{(f - f_{\mathrm{SW}})^2}{\sigma_{\mathrm{SW}}^2} \right], \tag{27}$$

where A_{SW} is the estimated amplitude of the surface wave hump, f_{SW} its central frequency, and σ_{SW} its spectral half-width.

The variations of f_{SW} and σ_{SW} with the roughness scale h are depicted in Fig. 18. As observed above, the central frequency decreases with h, approximately as $h^{-0.9}$, while in the linear regime it varies as $h^{-0.5}$ [see (26)]. The spectral half-width also tends to reduce with the roughness scale, almost linearly.

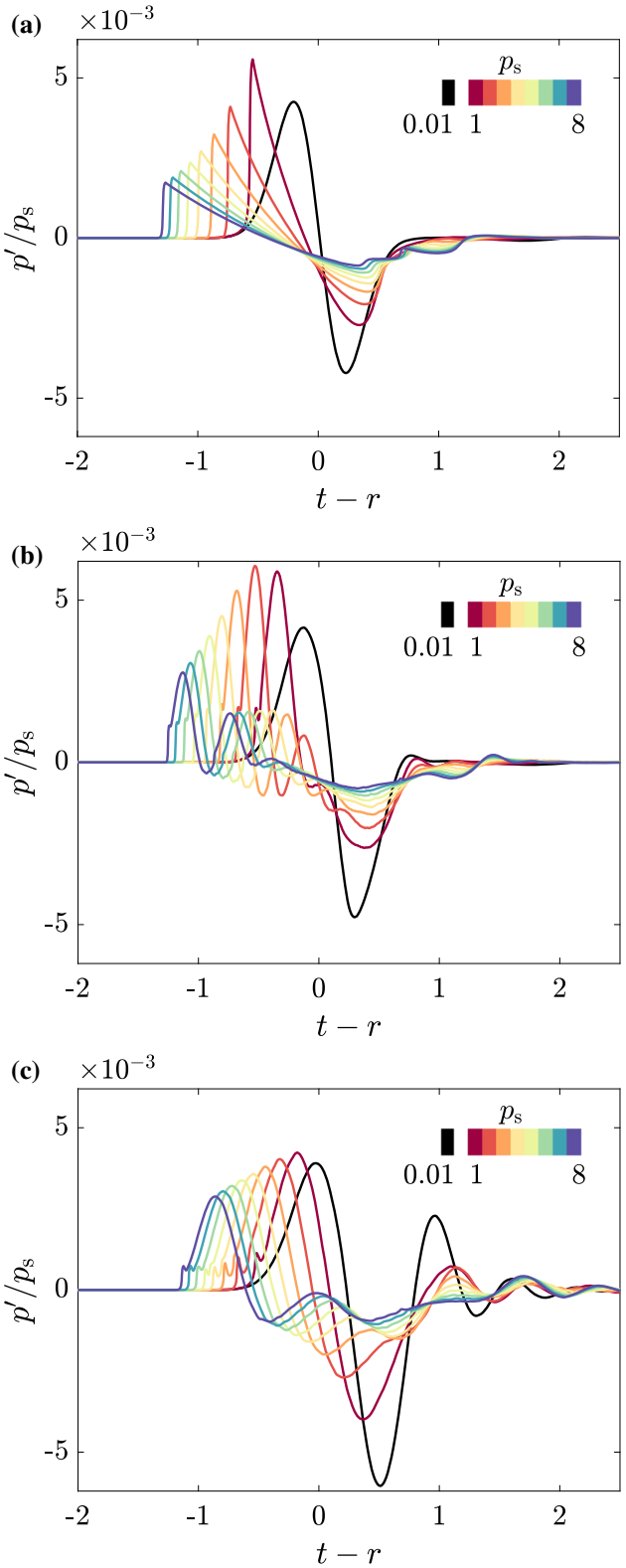

Fig. 19 Waveforms at $r = 30$ and $z = 0.2$ **a** for a smooth surface and for rough surfaces with **b** $h = 0.02$ and **c** $h = 0.05$ and for source amplitudes between 0.01 and 8

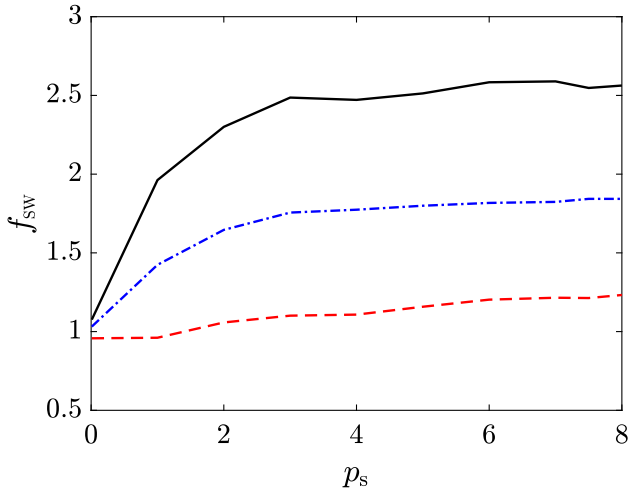

Fig. 20 Estimated central frequency of the surface wave spectrum as a function of the source amplitude for (solid) $h = 0.02$, (dash-dotted) $h = 0.03$, and (dashed) $h = 0.05$

4.2.3 Effect of the source characteristics

In this section, the evolution of the surface wave with the source characteristics, notably the source amplitude, is investigated.

The waveforms of overpressure are shown in Fig. 19 for several source amplitudes and for three surface conditions, namely a smooth surface and two rough surfaces with $h = 0.02$ and 0.05, at $r = 30$ and $z = 0.2$. For the smooth surface, the increase in source amplitude induces, first, the appearance of the shock discontinuity from $p_s = 1$ and then a lengthening of the waveform. Concerning the rough surfaces, for $h = 0.02$ and $p_s \geq 1$, the shock discontinuity is observed similarly and it is followed by the oscillations originating from the surface wave. The number of oscillations increases with p_s, and the period seems to decrease. As observed for the smooth surface, the signal lengthens with p_s. For $h = 0.05$, also note the presence of oscillations whose number tends to increase with p_s. Their period does not seem to vary with p_s. Finally, the oscillations at the tail of the waveform observed in the linear regime are still noticed for $p_s \geq 1$.

The procedure described in Sect. 4.2.2 to extract the characteristics of the surface waves is applied. The estimated central frequency of the surface wave is plotted as a function of the source amplitude in Fig. 20. Note that for $p_s = 0.01$, the value given by (26) has been used. The variations of the central frequency with source amplitude are significant mostly for $p_s \leq 3$. For $p_s \geq 3$, it slowly increases with the source amplitude in the three cases.

Besides, the waveforms were obtained for a particular source. In order to verify that this surface wave component is a general feature that should be expected for weak blast wave propagation above a rough surface, additional simulations

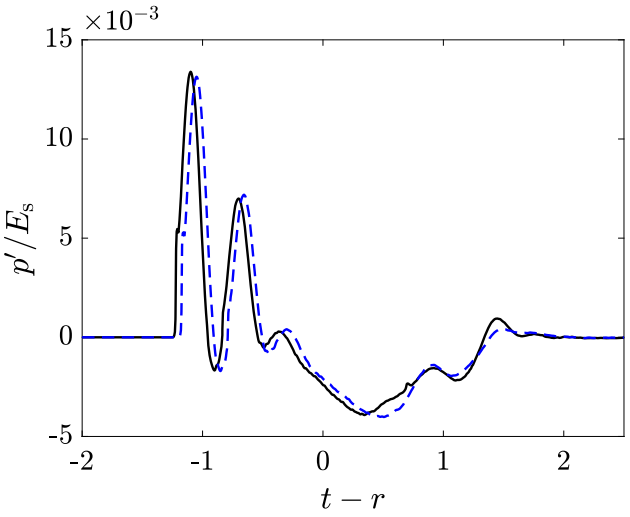

Fig. 21 Waveforms of the overpressure for $h = 0.02$ at $r = 30$ and $z = 0.2$ for two sources with the same energy (solid) $p_s = 7.5$ and $B = 0.25$ and (dashed) $p'_s = p_s/2$ and $B' = 2^{1/3}B$

have been conducted for a source with a reduced amplitude $p'_s = p_s/2$ and an increased half-width $B' = 2^{1/3}B$ (to keep the same source energy $E'_s = E_s$). Figure 21 shows an example of the waveforms for $h = 0.02$ at $r = 30$ and $z = 0.2$ obtained with the two sets of coefficients of the source. While the details of the waveforms differ, the oscillations related to the surface wave persist, which tends to confirm that surface waves are excited by weak blast waves over a rough surface.

5 Conclusions

The propagation of weak spherical blast waves above a rough periodic surface has been studied. To do so, numerical simulations of the Euler equations have been carried out. A detailed analysis of the reflection pattern has been performed. It has been shown that the waves diffracted by the rough surface combine to form an effective reflected shock that is first detached from the incident shock. For a sufficiently large source energy, it may interact with the incident shock and induce a Mach reflection pattern. Compared to a smooth surface, the appearance of the Mach stem is delayed and its height is reduced as if the source was of smaller amplitude and at a larger distance. For large roughness scales, the incident and reflected shocks remain detached. As weak blast waves degenerate to sound waves at long range, this behavior is expected to persist even for larger distances than those simulated. The variation of the peak overpressure with roughness scale has also been investigated. Near the surface, the peak pressure is larger for small roughness scales than for a smooth surface, but it is comparable or smaller far from the surface in all cases. The increase in peak pressure is related to oscillations that appear on the waveforms behind the shock. These properties have been associated with the presence of a surface wave that propagates along the rough surface. A comparison with an analytical solution in the linear regime has confirmed its existence. The evolution of the surface wave properties with the source amplitude has thus been examined, showing that an increase in source amplitude induces a shift toward higher frequencies.

There are several directions in which this work can be continued. This kind of simulations can be used to develop or extend empirical formula to account for roughness in predicting triple-point trajectory, as done recently by Xiao et al. [38] for a smooth and flat surface.

Furthermore, as axisymmetric roughness has been considered, an extension would be to perform simulations for a more realistic two-dimensional roughness. In addition, the roughness has been characterized by a single parameter, as, for simplicity, the roughness width was set to two times its height. Effect of these two parameters on the reflection of spherical weak blast waves could be investigated separately. Viscosity and thermal conduction have also been neglected. Nevertheless, in the experiments of Adachi et al. [20] for a plane shock wave impinging on a crenellated wedge (with a Mach number, however, larger than those considered in this work), schlieren pictures show the generation of vortices every time the plane shock wave passes above a roughness element. This should bring extra dissipation, not accounted for in the paper. This would also require to perform simulations with two-dimensional roughness to avoid generating unrealistic vortex rings and with a finer mesh near the walls to accurately capture the boundary layer.

Moreover, an effective boundary condition has been recently proposed for time-domain simulations in linear acoustics [39] to avoid the extra cost due to a fine mesh at a rough surface. It would thus be worthwhile to apply this boundary condition to spherical blast waves and investigate its range of validity in terms of Mach number.

Supplementary Information The online version contains supplementary material available at https://doi.org/10.1007/s00193-021-01024-8.

Acknowledgements This work was performed within the framework of the Labex CeLyA of the Université de Lyon, within the program "Investissements d'Avenir" (ANR-10-LABX-0060/ANR-16-IDEX-0005) operated by the French National Research Agency (ANR). It was also supported by LETMA (Laboratoire ETudes et Modélisation Acoustique), a Contractual Research Laboratory shared between CEA, CNRS, Ecole Centrale de Lyon, C-Innov, and Sorbonne Université. It was granted access to the HPC resources of PMCS2I (Pôle de Modélisation et de Calcul en Sciences de l'Ingénieur et de l'Information) of Ecole Centrale de Lyon, PSMN (Pôle Scientifique de Modélisation Numérique) of ENS de Lyon, and P2CHPD (Pôle de Calcul Hautes Performances Dédiés) of Université Lyon I, members of FLMSN (Fédération Lyonnaise de Modélisation et Sciences Numériques), partner of EQUIPEX EQUIP@MESO, and to the resources of IDRIS (Institut du Développement et des Ressources en Informatique Sci-

entifique) under the allocation 2019-02203 made by GENCI (Grand Equipement National de Calcul Intensif).

Appendix 1: Grid convergence

In this appendix, results of a grid convergence study are presented. A rough surface with $h = 0.01$ is considered. It corresponds to the smallest roughness scale investigated, with the least number of points per period. It is thus the most restrictive case. Simulations are performed for five grid sizes along the ξ-direction, ranging from $\Delta\xi = 1 \times 10^{-3}$ to 2×10^{-3}, with 1.5×10^{-3} being the reference grid size used in the paper. The number of points per period of the rough surface $2h/\Delta\xi$ is thus between 10 (for $\Delta\xi = 2 \times 10^{-3}$) and 20 (for $\Delta\xi = 1 \times 10^{-3}$). For all simulations, the grid size along the η-direction is 4×10^{-3} and the CFL number is set to 0.28.

The waveforms of the overpressure at $r = 30$ and $z = 0.2$ are plotted in Fig. 22 for the five grid sizes. Overall, an excellent agreement is obtained for the different grid sizes. In particular, the peak overpressure only fluctuates by 4% between the finest mesh and the coarsest mesh. The effect of the grid size on the waveforms can be noticed on the oscillations after the first peak, whose period is about 0.18. They appear smoothed for the coarsest mesh, and their peak-to-peak amplitude slightly increases with the reduction in the grid size.

The corresponding energy spectral densities are shown in Fig. 23. Here as well, the curves show only little dependence on the grid size. The main difference is observed on the amplitude of the hump near $f = 5.5$, which is related to the oscillations on the waveforms discussed on the previous paragraph.

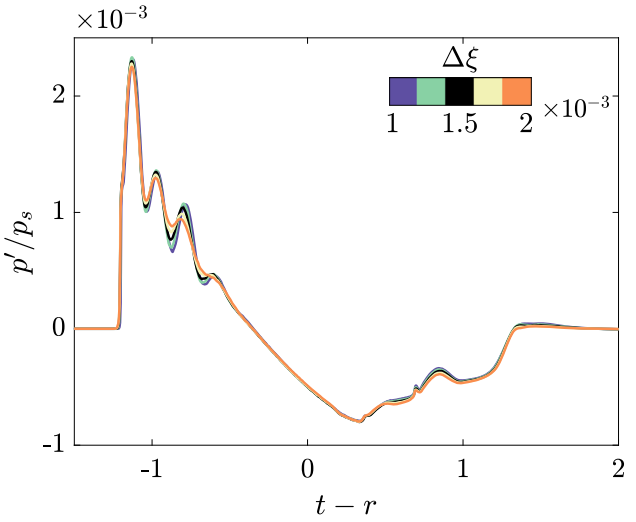

Fig. 22 Waveforms of the overpressure for $h = 0.01$ at $r = 30$ and $z = 0.2$ for several grid sizes

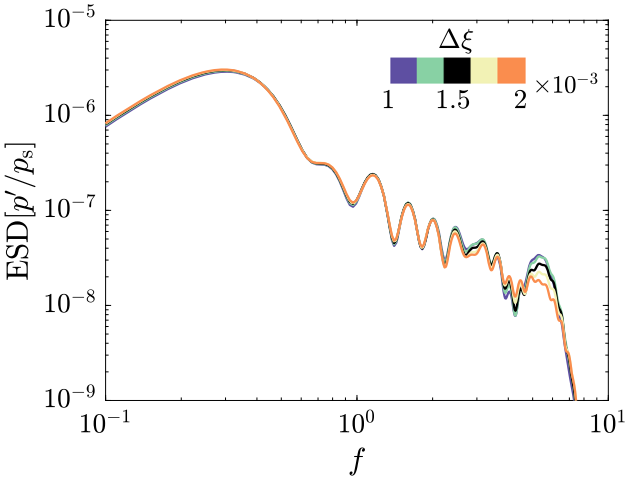

Fig. 23 Energy spectral density for $h = 0.01$ at $r = 30$ and $z = 0.2$ for several grid sizes

Additional convergence tests have been performed for roughness scales of $h = 0.02$ with the same grid sizes than for $h = 0.01$ and of $h = 0.15$ with grid sizes $\Delta\xi$ between 2×10^{-3} and 3×10^{-3}. Results are not shown for conciseness. The waveforms and the energy spectral densities present even smaller differences with the different grid sizes than for the case exemplified in Figs. 22 and 23.

In conclusion, the grid convergence study has shown that the results in terms of waveforms and spectra only marginally depend on the grid size. This demonstrates that grid convergence is obtained with the mesh used in the study.

Appendix 2: Effective admittance

Several methods have been proposed in the literature for deriving effective admittance of rough surfaces. Among

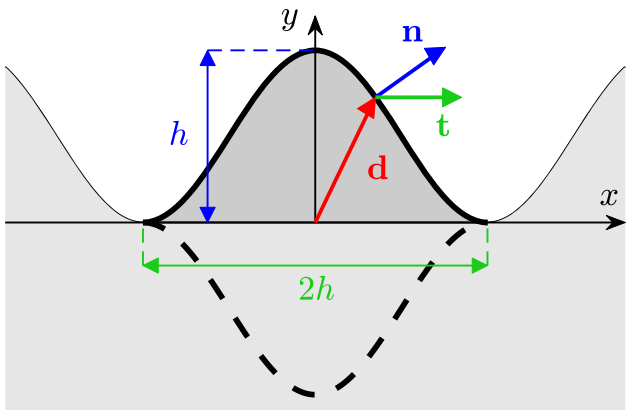

Fig. 24 Definition of the parameters to calculate I in the boss model

them, the boss model [9,36] is especially well suited for rough periodic surfaces. In this model, the rough surface is composed of identical roughness elements with a characteristic size h placed on an underlying smooth surface and spaced apart by a distance b.

For a 1D rough periodic surface at low frequencies ($\omega h < \omega b \leq 1$), the effective admittance can be written at grazing incidence as [9,36]:

$$\beta(\omega) = -\mathrm{i}\omega\epsilon, \tag{28}$$

where ϵ is related to the geometric properties of the rough surface via:

$$\epsilon = V\left(\frac{1+K}{\nu} - 1\right), \tag{29}$$

with ν given by:

$$\nu = 1 + \frac{\pi}{3} V \frac{1+K}{b}. \tag{30}$$

The parameter V is the cross-sectional area of the roughness elements above the smooth plane per unit length, and K is a hydrodynamic factor that depends on the shape of the roughness element. Following Tolstoy [36] and Lauriks et al. [40], it can be determined by the relation $K = I/(1-I)$ with:

$$I = \frac{1}{\pi}\int_L \frac{\mathbf{d}\cdot\mathbf{t}}{|\mathbf{d}|^2}\mathrm{d}\mathbf{L}\cdot\mathbf{t}, \tag{31}$$

where the integral is performed along the surface of the roughness element. In the above equation, $\mathbf{t}$ denotes the vector tangent to the smooth plane and $\mathbf{d}$ the vector between the centroid of the roughness element plus its image by the smooth plane and a point on the surface of the roughness element (Fig. 24). Setting $\mathbf{t} = (1,0)$ and using the parametrization $\mathbf{d} = (x(t), y(t))$ with $a \leq t \leq c$, one has $\mathrm{d}\mathbf{L} = (-y'(t), x'(t))\,\mathrm{d}t$, which yields:

$$I = -\frac{1}{\pi}\int_a^c \frac{x(t)\,y'(t)}{x^2(t)+y^2(t)}\,\mathrm{d}t. \tag{32}$$

The profile in (1) is modeled as a 1D rough surface with roughness elements of sinusoidal shape and of width $2h$ separated by a distance $2h$. This corresponds to $b = 2h$ and $V = h/2$. For determining K, the parametrization $x(t) = ht$ and $y(t) = h/2[1+\cos(\pi t)]$ for $-1 \leq t \leq 1$ is chosen. This gives:

$$I = \frac{1}{2}\int_{-1}^{1} \frac{t\sin(\pi t)}{t^2+\cos^4(\pi t/2)}\mathrm{d}t \approx 0.55. \tag{33}$$

Combining the values of the different parameters to determine ϵ in (29) finally leads to (20).

References

1. Kinney, G.F., Graham, K.J.: Explosive Shocks in Air, 2nd edn. Springer, New York (1985)
2. Ben-Dor, G.: Shock Wave Reflection Phenomena, 2nd edn. Springer, Berlin (2007)
3. Dewey, J.M., McMillin, D.J.: Photogrammetry of spherical shocks reflected from real and ideal surfaces. J. Fluid Mech. **81**(4), 701–717 (1977). https://doi.org/10.1017/S0022112077002304
4. Dewey, J.M., McMillin, D.J.: An analysis of the particle trajectories in spherical blast waves reflected from real and ideal surfaces. Can. J. Phys. **59**(10), 1380–1390 (1981). https://doi.org/10.1139/p81-182
5. Huber, P.W., McFarland, D.R.: Effect of surface roughness on characteristics of spherical shock waves. NASA Technical Report R-23, pp. 1–25 (1959)
6. Needham, C.E.: Blast Waves, 2nd edn. Springer, New York (2018)
7. Karzova, M.M., Lechat, T., Ollivier, S., Dragna, D., Yuldashev, P.V., Khokhlova, V.A., Blanc-Benon, P.: Effect of surface roughness on nonlinear reflection of weak shock waves. J. Acoust. Soc. Am. **146**(5), EL438-433 (2019). https://doi.org/10.1121/1.5133737
8. Qin, Q., Attenborough, K.: Characteristics and application of laser-generated acoustic shock waves in air. Appl. Acoust. **65**(4), 325–340 (2004). https://doi.org/10.1016/j.apacoust.2003.11.003
9. Attenborough, K., Li, K.M., Horoshenkov, K.: Predicting Outdoor Sound. Taylor & Francis, London (2007)
10. Boulanger, P., Attenborough, K.: Effective impedance spectra for rough sea effects on atmospheric impulsive sounds. J. Acoust. Soc. Am. **117**(2), 751–762 (2005). https://doi.org/10.1121/1.1847872
11. Donato, R.J.: Model experiments on surface waves. J. Acoust. Soc. Am. **63**(3), 700–703 (1978). https://doi.org/10.1121/1.381797
12. Daigle, G.A., Stinson, M.R., Havelock, D.I.: Experiments on surface waves over a model impedance plane using acoustical pulses. J. Acoust. Soc. Am. **99**(4), 1993–2005 (1996). https://doi.org/10.1121/1.415386
13. Bashir, I., Taherzadeh, S., Attenborough, K.: Surface waves over periodically-spaced rectangular strips. J. Acoust. Soc. Am. **134**(6), 4691–4697 (2013). https://doi.org/10.1121/1.4824846
14. Berry, D.L., Taherzadeh, S., Attenborough, K.: Acoustic surface wave generation over rigid cylinder arrays on a rigid plane. J. Acoust. Soc. Am. **146**(4), 2137–2144 (2019). https://doi.org/10.1121/1.5126856
15. Duff, R.E.: The interaction of plane shock waves and rough surfaces. J. Appl. Phys. **23**(12), 1373–1379 (1952). https://doi.org/10.1063/1.1702077
16. Takayama, K., Gotoh, J., Ben-Dor, G.: Influence of surface roughness on the shock transition in quasi-stationary and truly non-stationary flows. In: Treanor, C.E., Hall, J.G. (eds.) Shock Tubes and Waves, Proceedings of the 13th International Symposium on Shock Tubes and Waves, Niagara Falls, NY, pp. 326–334 (1981)
17. Takayama, K., Ben-Dor, G., Gotoh, J.: Regular to Mach reflection transition in truly nonstationary flows–influence of surface roughness. AIAA J. **19**(9), 1238–1240 (1981). https://doi.org/10.2514/3.7852
18. Ben-Dor, G., Mazor, G., Takayama, K., Igra, O.: Influence of surface roughness on the transition from regular to Mach reflection in pseudo-steady flows. J. Fluid Mech. **176**, 333–356 (1987). https://doi.org/10.1017/S0022112087000703
19. Reichenbach, H.: Roughness and heated layer effects on shock wave propagation and reflection—experimental results. Ernst-Mach-Institut, Rep. E25/85 (1985)
20. Adachi, T., Kobayashi, S., Suzuki, T.: An experimental analysis of oblique shock reflection over a two-dimensional multi-guttered wedge. Fluid Dyn. Res. **9**(5), 119–132 (1992). https://doi.org/10.1016/0169-5983(92)90062-2

21. Suzuki, T., Adachi, T., Kobayashi, S.: Experimental analysis of reflected shock behavior over a wedge with surface roughness. JSME Int. J. Ser. B Fluids Therm. Eng. **36**(1), 130–134 (1993). https://doi.org/10.1299/jsmeb.36.130
22. Gal-Chen, T., Sommerville, R.C.J.: On the use of a coordinate transformation for the solution of the Navier-Stokes equations. J. Comp. Phys. **17**, 209–228 (1975). https://doi.org/10.1016/0021-9991(75)90037-6
23. Salomons, E.M., Blumrich, R., Heimann, D.: Eulerian time-domain model for sound propagation over a finite-impedance ground surface. Comparison with frequency-domain models. Acta Acust. Acust. **88**(4), 483–492 (2002)
24. Bogey, C., Bailly, C.: Three-dimensional non-reflective boundary conditions for acoustic simulations: far field formulation and validation test cases. Acta Acust. Acust. **88**(4), 463–471 (2002)
25. Mohseni, K., Colonius, T.: Numerical treatment of polar coordinate singularities. J. Comput. Phys. **157**(2), 787–795 (2000). https://doi.org/10.1006/jcph.1999.6382
26. Bogey, C., Bailly, C.: A family of low dispersive and low dissipative explicit schemes for flow and noise computations. J. Comput. Phys. **194**(1), 194–214 (2004). https://doi.org/10.1016/j.jcp.2003.09.003
27. Bogey, C., de Cacqueray, N., Bailly, C.: A shock-capturing methodology based on adaptative spatial filtering for high-order non-linear computations. J. Comput. Phys. **228**(5), 1447–1465 (2009). https://doi.org/10.1016/j.jcp.2008.10.042
28. Berland, J., Bogey, C., Marsden, O., Bailly, C.: High-order, low dispersive and low dissipative explicit schemes for multiple-scale and boundary problems. J. Comput. Phys. **224**(2), 637–662 (2007). https://doi.org/10.1016/j.jcp.2006.10.017
29. Sabatini, R., Marsden, O., Bailly, C., Bogey, C.: A numerical study of nonlinear infrasound propagation in a windy atmosphere. J. Acoust. Soc. Am. **140**(1), 641–656 (2016). https://doi.org/10.1121/1.4958998
30. Berland, J., Bogey, C., Bailly, C.: Low-dissipation and low-dispersion fourth-order Runge-Kutta algorithm. Comput. Fluids **35**(10), 1459–1463 (2006). https://doi.org/10.1016/j.compfluid.2005.04.003
31. Karzova, M.M., Lechat, T., Ollivier, S., Dragna, D., Yuldashev, P.V., Khokhlova, V.A., Blanc-Benon, P.: Irregular reflection of spark-generated shock pulses from a rigid surface: Mach–Zehnder interferometry measurements in air. J. Acoust. Soc. Am. **145**(1), 26–35 (2019). https://doi.org/10.1121/1.5084266
32. Emmanuelli, A., Dragna, D., Ollivier, S., Blanc-Benon, P.: Characterization of topographic effects on sonic boom reflection by resolution of the Euler equations. J. Acoust. Soc. Am. **149**(4), 2437–2450 (2021). https://doi.org/10.1121/10.0003816
33. Boutillier, J., Ehrhardt, L., De Mezzo, S., Deck, C., Magnan, P., Naz, P., Willinger, R.: Evaluation of the existing triple point path models with new experimental data: proposal of an original empirical formulation. Shock Waves **28**, 243–252 (2018). https://doi.org/10.1007/s00193-017-0743-7
34. Reed, J.W.: Atmospheric attenuation of explosion waves. J. Acoust. Soc. Am. **61**(39), 39–47 (1977). https://doi.org/10.1121/1.381266
35. Dragna, D., Blanc-Benon, P., Poisson, F.: Time-domain solver in curvilinear coordinates for outdoor sound propagation over complex terrain. J. Acoust. Soc. Am. **133**(6), 3751–3763 (2013). https://doi.org/10.1121/1.4803863
36. Tolstoy, I.: Smoothed boundary conditions, coherent low-frequency scatter, and boundary modes. J. Acoust. Soc. Am. **75**(1), 1–22 (1984). https://doi.org/10.1063/1.1666645
37. Habault, D., Filippi, P.J.T.: Ground effect analysis: surface wave and layer potential representations. J. Sound Vib. **79**(4), 529–550 (1981). https://doi.org/10.1016/0022-460X(81)90464-8
38. Xiao, W., Andrae, M., Gebbeken, N.: Development of a new empirical formula for prediction of triple point path. Shock Waves **30**, 677–686 (2020). https://doi.org/10.1007/s00193-020-00968-7
39. Faure, O., Gauvreau, B., Junker, F., Lafon, P., Bourlier, C.: Modelling of random ground roughness by an effective impedance and application to time-domain methods. Appl. Acoust. **119**, 1–8 (2017). https://doi.org/10.1016/j.apacoust.2016.11.019
40. Lauriks, W., Kelders, L., Allard, J.F.: Surface waves above gratings having a triangular profile. Ultrasonics **36**(8), 865–871 (1998). https://doi.org/10.1016/S0041-624X(98)00009-2